REPORT DOCUMENTATION PAGE

Form Approved
OMB No. 0704-0188

1. REPORT DATE *(DD-MM-YYYY)*	**2. REPORT TYPE**	**3. DATES COVERED** *(From - To)*
December 2013	Technical Paper	December 2013

4. TITLE AND SUBTITLE
Development of a Facility for Combustion Stability Experiments at Supercritical Pressure

5a. CONTRACT NUMBER
In-House

5b. GRANT NUMBER

5c. PROGRAM ELEMENT NUMBER

6. AUTHOR(S)
Wegener, Leyva, Forliti, Talley

5d. PROJECT NUMBER

5e. TASK NUMBER

5f. WORK UNIT NUMBER
Q0YA

7. PERFORMING ORGANIZATION NAME(S) AND ADDRESS(ES)

Air Force Research Laboratory (AFMC)
AFRL/RQRC
10 E. Saturn Blvd.
Edwards AFB CA 93524-7680

8. PERFORMING ORGANIZATION REPORT NO.

9. SPONSORING / MONITORING AGENCY NAME(S) AND ADDRESS(ES)
Air Force Research Laboratory (AFMC)
AFRL/RQR
5 Pollux Drive
Edwards AFB CA 93524-7048

10. SPONSOR/MONITOR'S ACRONYM(S)

11. SPONSOR/MONITOR'S REPORT NUMBER(S)
AFRL-RQ-ED-TP-2013-265

12. DISTRIBUTION / AVAILABILITY STATEMENT
Distribution A: Approved for Public Release; Distribution Unlimited. PA#13550

13. SUPPLEMENTARY NOTES
Conference Paper for the AIAA 52nd Aerospace Sciences Meeting, National Harbor, MD, 13-17 January 2014.

14. ABSTRACT

Combustion instability in liquid rocket engines can have severe consequences including degraded performance, accelerated component wear, and potentially catastrophic failure. High-frequency instabilities, which are generally the most harmful in liquid rocket engines, can be driven by interactions between disturbances associated with transverse acoustic resonances and the combustion process. The combustion response to acoustic perturbation is a critical component of the instability mechanism, and is in general not well understood. The current paper describes an experimental facility at the Air Force Research Laboratory (AFRL) at Edwards Air Force Base that is intended to investigate the coupling between transverse acoustic resonances and single/multiple liquid rocket engine injector flames. Critical aspects of the facility will be described, including the capability to operate at supercritical pressures that are relevant to high-performance liquid rocket engines, accurately-controlled and cryogenically-conditioned propellants, and optical access to facilitate the use of advanced diagnostics. The transverse acoustic resonance is induced through the use of carefully-controlled piezo-sirens, allowing monochromatic excitation across a range of amplitudes at a number of discrete frequencies. The location of the flame within the acoustic resonance mode shape can also be varied through relative phase control of the two acoustic sources. The operating space of the facility, for oxygen and hydrogen operation, will be described. Preliminary non-reacting and reacting data will also be presented to demonstrate the quality of operation of this facility. It is anticipated that future results generated using this facility will provide both fundamental insight into the acoustic-flame interactions as well as provide a database useful for validating combustion instability models.

15. SUBJECT TERMS

16. SECURITY CLASSIFICATION OF:			**17. LIMITATION OF ABSTRACT**	**18. NUMBER OF PAGES**	**19a. NAME OF RESPONSIBLE PERSON**
					Doug Talley
a. REPORT	**b. ABSTRACT**	**c. THIS PAGE**	SAR	21	**19b. TELEPHONE NO** *(include area code)*
Unclassified	**Unclassified**	**Unclassified**			661-525-6174

Standard Form 298 (Rev. 8-98)
Prescribed by ANSI Std. 239.18

Development of a Facility for Combustion Stability Experiments at Supercritical Pressure

Jeffrey L. Wegener[1]
University of California at Los Angeles, CA 90095

Ivett A. Leyva[2]
AFRL/RQRE, Edwards AFB, CA 93524

David J. Forliti[3]
Sierra Lobo, Inc. supporting AFRL/RQRC, Edwards AFB, CA 93524

and
Douglas G. Talley[4]
AFRL/RQRC, Edwards AFB, CA 93524

Combustion instability in liquid rocket engines can have severe consequences including degraded performance, accelerated component wear, and potentially catastrophic failure. High-frequency instabilities, which are generally the most harmful in liquid rocket engines, can be driven by interactions between disturbances associated with transverse acoustic resonances and the combustion process. The combustion response to acoustic perturbation is a critical component of the instabililty mechanism, and is in general not well understood. The current paper describes an experimental facility at the Air Force Research Laboratory (AFRL) at Edwards Air Force Base that is intended to investigate the coupling between transverse acoustic resonances and single/multiple liquid rocket engine injector flames. Critical aspects of the facility will be described, including the capability to operate at supercritical pressures that are relevant to high-performance liquid rocket engines, accurately-controlled and cryogenically-conditioned propellants, and optical access to facilitate the use of advanced diagnostics. The transverse acoustic resonance is induced through the use of carefully-controlled piezo-sirens, allowing monochromatic excitation across a range of amplitudes at a number of discrete frequencies. The location of the flame within the acoustic resonance mode shape can also be varied through relative phase control of the two acoustic sources. The operating space of the facility, for oxygen and hydrogen operation, will be described. Preliminary nonreacting and reacting data will also be presented to demonstrate the quality of operation of this facility. It is anticipated that future results generated using this facility will provide both fundamental insight into the acoustic-flame interactions as well as provide a database useful for validating combustion instability models.

Nomenclature

A	=	area
c	=	speed of sound
D_1	=	inner injector inner diameter
D_2	=	inner injector outer diameter

[1] Graduate Student, Department of Mechanical and Aerospace Engineering, UCLA, Los Angeles, CA 90095 student member.
[2] Technical Advisor, AFRL/RQRE, 4 Draco Drive, Building 8351, Edwards AFB, CA 93524, Associate Fellow.
[3] Research Scientist, Sierra Lobo, Inc., 4 Draco Drive, Building 8451, Edwards AFB, CA 93524, senior member.
[4] Lead, Combustion Dynamics Group, AFRL/RQRC., 4 Draco Drive, Building 8451, Edwards AFB, CA 93524, Associate Fellow.

D_3 = outer injector inner diameter
D_4 = outer injector outer diameter
dt = time step
f_F = acoustic frequency
m = waveguide flare constant
p_c = mean chamber pressure
p' = acoustic pressure perturbation amplitude
t = inner post thickness
u' = acoustic velocity perturbation amplitude
x = streamwise (longitudinal) coordinate axis
y = spanwise (transverse) coordinate axis
z = depthwise coordinate axis

I. Introduction

LIQUID rocket engines exhibit challenging scientific problems which have been the subject of extensive efforts over several decades. A fundamental understanding of these problems remains incomplete for several phenomena, with combustion instability being a critical example. This lack of understanding has caused delays and budget increases in rocket engine development programs. The inability to predict combustion instabilities in particular, requires expensive iterative testing as part of the development cycle.

Physics-based modeling and understanding of the problem have potential to improve the prediction of combustion instability, leading to a simplified design cycle requiring fewer redesign iterations. Verification and validation of numerical models for combustion stability require advanced bench-scale experiments to serve two primary purposes. First, these experiments must improve fundamental knowledge of the underlying physics of combustion instability. Combustion instability has been investigated in a wide range of scenarios and typically involves a coupling between hydrodynamic instabilities, unsteady heat release, and acoustic disturbances[1]. Liquid rocket engine (LRE) injectors create non-premixed flames, relying on turbulent mixing within shear layers which exhibit velocity and heat release oscillations that can couple with chamber acoustics. Characterizing these oscillations in terms of frequencies and amplitudes from detailed experimental measurements and data analysis will improve the ability to predict these values, and indicate the likelihood of an oscillation giving rise to combustion instability. Second, these experiments must provide data for validation of computational models. This requirement drives the need for high-fidelity measurements and well-characterized boundary conditions.

Fundamental experiments exploring combustion stability in conditions similar to that of a liquid rocket engine (LRE) require challenging systems, including cryogenic propellants and supercritical chamber pressure operation, among others. To meet these requirements, a new combustion stability experimental facility was recently constructed at the Air Force Research Laboratory (AFRL) at Edwards Air Force Base. The development of this facility was based on experience gained from an existing nonreactive facility at AFRL[2-4]. Insight was also gained from a small number of existing combustors which create LRE conditions in sub-scale tests. These tests involve total mass flow rates which are often orders of magnitude lower than a typical LRE and contain five or fewer injector elements. But, in order to employ detailed experimental methods, such as high-speed diagnostics and acoustic control systems, a variety of hardware designs have been used. Five modern combustors are particularly relavant for comparison with the new combustion stability facility. These are the Multi-injector Combustor (MIC) and the Very High Amplitude Modulator (VHAM) facility, both operated jointly by ONERA and CNRS, the Common Research Combustor (CRC) operated jointly by CNRS and DLR, the BKH combustor operated by DLR, and the Continuously Variable Resonance Combustor (CVRC) operated by Purdue University.

The CRC originated in 2002 from the efforts of a German-French working group which now operates identical experimental combustors at the Research Institute for Equilibrium Systems (IRPHE) in Marseilles, France and DLR in Lampoldshausen, Germany. The CRC injects propellant from one side of a flat, cylindrically shaped chamber through a single injector which is $1/10^{th}$ scale of a typical LRE injector. With high-speed shadowgraphy and OH* chemiluminescence imaging, the dynamics of a single LOx/H_2 flame were investigated to fundamentally relate spatial and temporal heat release oscillations to pressure oscillations controlled by external acoustic forcing. A single injector element though, provides only partial representation of thermoacoustic instabilities occurring in LREs that contain multiple injectors and interactions between adjacent flames.

The BKH combustor is part of a recently constructed facility at DLR Lampoldshausen, Germany, which focuses on high-frequency combustion instability for LO_x/H_2 conditions[5,6]. This combustor includes five shear coaxial injectors in a cross formation to investigate interactions between neighboring flames. The MIC, located in Paris, France, shares many design features with the BKH combustor. The MIC uses multiple injectors, but in a linear arrangement to isolate interactions between pairs of flames using two-dimensional imaging[7,8]. Unless utilizing laser sheet flame illumination, a cross formation prevents one from distinguishing between foreground and background flames when viewing OH* emission images.

The VHAM facility is a modified version of the MIC which creates much greater acoustic pressure amplitudes in an effort to replicate the high-amplitude oscillations documented in actual LRE combustion instabilities[9]. The VHAM facility uses a toothed wheel to periodically block gas flow through exhaust nozzles, creating high-pressure amplitudes inside the combustion chamber. The toothed-wheel exhaust nozzle technique is also employed in the MIC, BKH, and CRC designs for the same purpose. With this method, the periodic nozzle imposes an acoustic boundary condition on the chamber wall, where the acoustic frequency is controlled by the wheel speed. The resulting pressure perturbation amplitude though, is not independently controlled, and is instead determined by hardware geometry such as nozzle diameter and tooth profile design. In the MIC, BKH, and CRC configurations, the toothed wheel is placed over a secondary exhaust nozzle which is located on the side of the chamber, perpendicular to the primary exhaust nozzle. The VHAM does not use secondary nozzles and two primary exhaust nozzles located at the end of the chamber are periodically blocked by a common toothed wheel. This alternative design was used to create pressure amplitudes as high as 20% of p_{cc} in the VHAM, whereas previous experience with the smaller amplitudes of the MIC design yielded limited flame response[9].

Controlled acoustic excitation in the manner described above allows a partial decoupling of a portion of the combustion instability feedback loop. Without an external acoustic source, chamber pressure perturbations exist due to combustion instabilities alone, and these natural changes in pressure cause further pulsations in combustion and heat release rate via oscillations in propellant flow and mixing rates. This mechanism is best represented in three steps as shown in Fig. 1. As flow oscillations represented by u' create fluctuations in propellant mixing, unsteady heat release is produced, represented by q' in Fig. 1. Then, unsteady heat release induces acoustic pressure perturbations which may resonate within the combustion chamber. Acoustics may influence the propellant mixing process and create a feedback mechanism. In this way, the flame serves as a source. But, when controlled acoustic excitation contributes to chamber acoustics, feedback dependencies are partly disassociated because a second source of acoustics is added. This allows one to investigate the effects of acoustic waves on fluid dynamic instability and unsteady heat release by varying acoustic pressure amplitude and frequency. With this strategy, the degree to which perturbation amplitudes and their inherent frequencies can be varied is highly dependent on the specific design used for external acoustic forcing.

In contrast to the nozzle modulation method used by all four aforementioned combustors, the CVRC of Purdue uses an acoustic control system relying on variable injector geometry[10]. By altering the size of the oxidizer plenum, the resonant frequency of the injector flow is controlled such that chamber pressure amplitudes range from less than 10% to 60% of the chamber pressure were achieved. The highest pressure amplitudes are achieved when the oscillation frequency of the injector matches the chamber pressure oscillation frequency, whereas a mismatch dampens the chamber mode. Thus, the CVRC design forgoes the electro-mechanical system of a typical acoustic source, and instead relies on injector flow oscillations to create heat release oscillations in the reaction zone. A family of chamber geometries can be investigated; some are stable and some are not. This method reliably induces high-amplitude instability, but requires mindful choice of fuel species and propellant flow conditions to indirectly manipulate the preferred frequency and amplitude of the instability.

The current endeavor concentrates on operational flexibility. The importance of variable injector configurations, propellant flow conditions, and acoustic excitation motivated the combustion stability facility design to offer a wide range of conditions in these three areas. A single injector is used in a modular flange, allowing for multiple injectors in future work. Second, propellant temperatures, and thus densities, are widely variable by employing cryogenic heat exchangers to cool ambient temperature gaseous propellants to the desired temperatures. Lastly, a pair of piezoelectric sirens serve as acoustic sources with variable acoustic pressure amplitudes and a range of forcing frequencies. This approach allows for separate control of amplitude and frequency.

II. Experimental Facility

The combustion stability facility takes on the complexities of a complete LRE test stand at subscale. All data acquisition and control system (DACS) hardware and user interfaces are located in a remote control room. Thus, the

infrastructure, plumbing, and electrical designs necessary to realize this facility are extensive. This description though, will be limited to features having a direct influence on the experimental environment. These include the combustion chamber, cryogenic heat exchangers and propellant supply systems, the acoustic excitation system, and high-speed imaging.

A. Combustion Chamber

Similar to the previously existing chamber used in nonreactive AFRL work[2,11], the chamber is designed as a chamber within another chamber. The inner chamber creates a near ideal environment for one-dimensional acoustic wave resonance, but is not sealed from the surrounding volume. This surrounding volume is the outer chamber, which has the structural integrity to withstand operating pressures of 1500 psi (=10.34 MPa). Thick walls and windows are not necessary for the inner chamber, allowing more freedom for placing injectors and integrating new injector designs. A CAD rendering of the chamber assembly is shown in Fig. 2, and a photograph of the completed facility is shown in Fig. 3 with the chamber integrated into the apparatus.

The outer chamber is fabricated from a forged Naval brass alloy and has an octagon shape to offer optical access from multiple views. The current configuration contains six windows, which includes large windows in the front and rear walls of the chamber and four smaller windows located at each corner of the outer chamber. The large windows are made of sapphire, while the smaller windows are made of quartz. Large opening in the two remaining chamber side walls are used for acoustic excitation attachments. The injector assembly and exhaust port are located at the top and bottom of the outer chamber, respectively, creating downward propellant flows which exit the combustor through a 4.8 mm exhaust orifice, the chamber's only exhaust path.

The central part of the inner chamber, where the injector is located, is a rectangular volume open to transverse acoustic excitation from the left and right. The inner chamber depth is 20.32 mm and the height is 36.07 mm, making room for subscale injectors only. The transverse width is much larger, reaching 0.82 m from the left acoustic source to the right acoustic source. This dimension makes the inner chamber volume large in comparison to the size of the combustion zone. One should also note that although the inner chamber cross sectional area is 20.32 mm × 36.07 mm near the injector, the far left and far right areas of the inner chamber expand to a large circular area in order to house each acoustic driver. Two quartz inner chamber windows separate the inner chamber from the outer chamber, and because these windows need not withstand a large pressure differential, small holes are located throughout the rear inner window. Hence dynamic pressure transducers and thermocouples are placed in these holes to diagnose the region near the flame by way of placement directly through the window. At the upper wall of the inner chamber, a gaseous nitrogen plenum provides two flows parallel to propellant flows. First, window cooling flows enter the inner chamber through slotted holes above the windows. Second, a propellant coflow system provides gaseous nitrogen to the region surrounding the flame by entering the chamber through dozens of 0.48 mm holes in a circular pattern around the injector.

B. Fluid Supply Systems

In a facility where propellant density control is crucial in achieving a set of experimental objectives, propellant temperature and pressure are paramount. In this case, the propellant pressure at the injector exit is treated as equal to the chamber pressure. The propellant temperature, though, is determined by the oxygen and hydrogen supply systems. Liquid rocket engine propellant tanks often hold fuel and oxidizer at cryogenic states, but this facility instead relies on ambient temperature propellant tanks providing high-pressure oxygen and hydrogen. Cryogenic heat exchangers then cool the propellants to the desired state. Thus, fluid supply system descriptions will focus on chamber pressurization techniques and cryogenic heat exchangers in order to understand propellant systems as a whole.

As in an LRE, similar experimental systems[5,9] have relied on combustion for chamber pressurization. But, when using subscale injectors and propellant flow rates of 10 g/s or less, combustion alone will not produce the high pressures seen in actual LREs. The current endeavor indeed maintains low flow rates, and also utilizes a relatively large chamber volume as explained in the previous section. Thus, an added source of mass flow must exist in order to achieve desired pressures and densities, which is a more precise technique to control the mean chamber pressure, rather than with combustion alone. A nitrogen chamber pressurization system serves this purpose by entering the chamber through multiple ports in the outer chamber wall, and chamber pressure is set using a variable control valve in the nitrogen supply system. Flow out of the chamber is restricted by the exhaust orifice. This technique adds freedom for designing a large array experimental conditions, because chamber pressure is controlled independent of propellant flow conditions. The source of chamber pressurization is partly decoupled from the combustion process.

With propellant pressure determined by chamber pressure, propellant flow rate and temperature are left to be controlled by the propellant feed system. First, flow rate is set using a remote needle valve followed by a mass flow meter (Porter 123 series), and both of these components are located upstream from the heat exchangers such that these components operate on gaseous propellants at nominal room temperature. Maximum mass flow rates are 0.7 g/s and 10 g/s for hydrogen and oxygen, respectively. Downstream of the flow meters, hydrogen and oxygen pass through individual heat exchangers. Both heat exchangers operate under similar principles where propellant flow passes through a coiled tube which is cooled by liquid nitrogen. The oxygen heat exchanger is shown in Fig. 4 and the hydrogen heat exchanger is shown in Fig. 5. In the case of the oxygen heat exchanger, the propellant tube is coiled inside of a casting which also contains a coiled tube for liquid nitrogen flow. Electric heaters are mounted to the aluminum casting to offer additional energy in the event that the casting is chilled below the target temperature. The heating system consists of six heater elements individually controlled by a closed-loop control system written in LabVIEW. In this way, coolant control valves are set to slightly sub-cool the casting using liquid nitrogen, reducing the process gas to a temperature 2 to 5 K below the target temperature. The heater power is then manually applied and automatically adjusted to hold the process fluid outlet temperature equal to the target temperature with an accuracy of ±1 K. The oxygen heat exchanger was designed and constructed by Sierra Lobo, Inc. For the hydrogen heat exchanger, the propellant tube is immersed directly within a liquid nitrogen bath and heaters are not included. The temperature of the process fluid in each heat exchanger is controlled by individually regulating liquid nitrogen flow rates through each system with separate control valves. Although the propellant heat exchangers offer variable control of temperature, a conditioning process is required to cool plumbing hardware prior to achieving a desired, stable temperature. The temperature conditioning process is performed using nitrogen as a surrogate process fluid in order to minimize propellant usage.

To characterize the capability of each heat exchanger, the minimum achievable temperature was measured for a range of chamber pressures. This was done by utilizing high liquid nitrogen flow rates over a long period of time to cool the hardware of each system. Thus, the injector flow temperature for each process fluid was minimized, representing a low temperature limit on the facility operating space. The results from this effort are shown in Fig. 6 for oxygen, where minimum temperature is shown to have a small dependence on chamber pressure. An oxygen density contour is the background of Fig. 6, showing that a liquid phase is achievable for $p_c < p_{crit,Ox}$, where $p_{crit,Ox}$ = 731 psia (=5.04 MPa). Mass flow rate is shown to have a negative correlation with temperature. Similar measurements were made with the hydrogen propellant system, but to perform these tests safely, helium was used as a surrogate. Minimum helium temperatures are shown in Fig. 7, superimposed on a hydrogen density contour map. For both oxygen and hydrogen, the minimum achievable temperature falls between 110 and 120 K with a primary dependence on propellant flow rate and a minor dependence on chamber pressure.

To formalize a range of possible operating conditions for the new facility, a parametric map of propellant density ratio S versus chamber pressure p_c is shown in Fig. 8. The oxygen and hydrogen density limits required to calculate S were determined using temperature limits from a heat exchanger characterization study. The upper temperature limit was taken as room temperature, while the lower limit is the minimum achievable propellant temperature ascertained from the heat exchanger characterization study, i.e. Figs. 6 and 7. To create Fig. 8, the resulting limits of S were then plotted for two-phase LO_x-GH_2 flow, single-phase GO_x-GH_2 flow, and flows in which $p_c > p_{crit,Ox}$.

The injector consists of a single shear-coaxial element designed for hydrogen flow in the annulus and oxygen flow in the center. In terms of total cross-sectional area, the injector is $1/10^{th}$ scale of the J-2 engine, for example. An injector of this size is challenging to manufacture, but is used here to achieve jet velocities and Reynolds numbers with an order of magnitude similar to an actual LRE while maintaining much smaller propellant mass flow rates. The cross sectional dimensions of the injector are shown in Fig. 9. The outer to inner jet area ratio is 1.68. The inner post thickness to inner diameter ratio t/D_1 has a value of 0.27, which prevents the inner shear layer from behaving purely as the meeting of co-flowing fluids. Instead, a recirculation zone is expected to form at the exit of the injector between the outer and inner jets. The length of the inner and outer injectors are sufficient to create fully developed turbulent flow at the exit for all conditions of interest here.

A comparison of the inner jet Reynolds number Re_{ij} and the outer jet Reynolds number Re_{oj} for similar research combustors is shown in Fig. 10, with operating points of actual oxygen-hydrogen LREs. Operating spaces of four other combustion instability research facilities are shown, including the BKH combustor of DLR, Germany, the Common Research Combustor (CRC) of CNRS, France and DLR, Germany, the Multi-Injector Combustor (MIC) of ONERA and CNRS, France, and the Cryogenic Combustion Laboratory (CCL) of Pennsylvania State University, USA. These facilities were specifically chosen for comparison because detailed flow conditions for oxygen-hydrogen stability experiments for shear-coaxial jets are available in published literature[5,7,8,12,13], but one must be cognizant that apparatuses such as these often see multiple modifications in only a few years time. As a result, Fig.

10 should be considered a general guide for comparison, because Re values for the facility concerned here, as well as the others in Fig. 10, can be revised with simple hardware modifications.

C. Acoustic Characterization

A challenging task required to complete the facility design was the development of an acoustic excitation system. An ideal design will offer free control of amplitude over a wide range of acoustic frequencies. But, as seen in the acoustic control systems of existing facilities[6], this proves to be difficult. Designs must often sacrifice either control of frequency or amplitude in order to achieve high pressure amplitudes on the order of those manifested by LRE combustion instabilities. This facility utilizes a pair of piezoelectric acoustic sirens, where pressure amplitude is variably controlled with input voltage amplitude until reaching the sirens maximum safe amplitude of approximately 600V. The chamber integrates the sirens using stainless steel waveguides mounted to the left and right sides of the outer chamber as shown in Fig. 2.

The waveguides act as horns which focus acoustic energy from the 100 mm diameter sirens to the smaller rectangular inner chamber. This acoustic horn technique facilitates the production of high pressure amplitudes at the point of interest, the flame. The waveguides' shape must provide a smooth transition from a 11.24 cm diameter circlular flange to a 2.03 cm × 3.61 cm rectangular cross-section. To minimize two-dimensional and three-dimensional waves, the circle-to-rectangle transition must be void of abrupt area changes and sharp corners. This requirement, combined with material stress from high chamber pressures, make design and fabrication challenging.

The area reduction from circle to rectangle follows a quasi-one-dimensional model for sound propagation in a rigid-walled duct, which is derived beginning with the acoustic wave equation,

$$\nabla^2 p - \frac{1}{c^2}\frac{\partial^2 p}{\partial t^2} = 0\,, \tag{1}$$

which is then integrated for acoustic pressure p for a three-dimensional segment of the duct. A coordinate system is adopted where x is the jet streamwise direction, y is the transverse direction, and z is the depthwise direction. Thus, a perfectly-shaped waveguide will prevent acoustic wave propagation in the x and z directions and concentrate 100% of the energy from each siren to produce waves in the y direction. Gauss's theorem is then used to convert the volume integral of $\nabla^2 p$ to a surface integral. Then, apply the boundary condition that $\nabla p \cdot n = 0$ at the inner wall of the waveguide, divide by Δy, and take the limit as $\Delta y \to 0$ ($\Delta y = \partial y$). One obtains

$$\frac{\partial}{\partial y}\iint_A \frac{\partial p}{\partial y}\,dA - \frac{1}{c^2}\frac{\partial^2}{\partial t^2}\iint_A p\,dA = 0\,. \tag{2}$$

With the exception of a thin acoustic boundary layer near the inner wall of the waveguide, p is uniform over any given cross section, i.e. $\frac{\partial p}{\partial x} = \frac{\partial p}{\partial z} = 0$. The equation above then reduces to

$$\frac{1}{A}\frac{\partial}{\partial y}\left(A\frac{\partial p}{\partial y}\right) - \frac{1}{c^2}\frac{\partial^2 p}{\partial t^2} = 0\,, \tag{3}$$

which is known as Webster's horn equation, after Arthur G. Webster[14]. Following Pierce[15], Webster's horn equation can be simplified as

$$\left\{\frac{\partial^2}{\partial y^2} + \frac{1}{4A^2}\left[(A')^2 - 2AA''\right] - \frac{1}{c^2}\frac{\partial}{\partial t^2}\right\}A^{1/2} p = 0\,. \tag{4}$$

This is a nonlinear ordinary differential equation with respect to A which can be used to describe the optimal area of an expanding or constricting waveguide. The general solution is

$$A = A_{th}\left(\cos my + T \sin my\right)^2 . \tag{5}$$

The specific solution is found for the catenoidal horn shape[15] for $T = 0$ using boundary conditions enforced by the chosen siren diameter, inner chamber area, and waveguide length in order to determine the throat area A_{th} and flare constant m. Finally, the specific solution was used to model the inside wall of each waveguide according to a prescribed area function. The CAD rendering in Fig. 11 shows the left waveguide in a cut-away view. With an identical assembly on the right of the chamber, the acoustic system produces high-amplitude pressure waves, $p'/p_c \sim 0.01$, traveling in the y direction.

Acoustic pressure amplitudes induced by this system are largely governed by the resonant modes of the chamber and the piezoelectric sirens. The chamber geometry will allow resonant modes for a particular set of acoustic frequencies, which are also dependent on the speed of sound for a given thermodynamics state. The sirens, on the other hand, have resonant frequencies of their own. Below 6 kHz, the sirens exhibit only three resonant frequencies and operating far from these three frequencies results in inefficient sound production and low pressure amplitudes. Thus the maximum achievable amplitudes are dependent on frequency as it relates to resonance of two independent phenomena.

Regarding the resonant chamber modes, an analytical examination reveals a broad array of frequencies. The analytical relationship between chamber length L, acoustic frequency f_F, and the speed of sound c follows as

$$L = \frac{n}{2}\lambda = \frac{n}{2}\left(\frac{c}{f_F}\right) \tag{6}$$

where even values of n create resonant conditions for acoustic sources operated in-phase (φ =0°) and odd values of n create resonant conditions for acoustic sources operated out-of-phase (φ =180°). In the same regard, sources operated in-phase will create a pressure antinode (PAN) at the center of the chamber and sources operated out-of-phase will create a pressure node (PN) at the center of the chamber. Due to the waveguides long span, ten transverse resonant frequencies occur at less then 6 kHz. Unlike convective waves, a resonant condition will form acoustic waves which are symmetric with respect to both space and time. Spatially, an isothermal volume subject to transverse resonance will produce evenly spaced PNs and PANs. This places the injector at a location of known acoustic perturbation gradients $\frac{\partial p'}{\partial y}$ and $\frac{\partial u'}{\partial y}$, where $\frac{\partial p'}{\partial y} = 0$ for a PAN condition (φ =0°) and $\frac{\partial u'}{\partial y} = 0$ for a PN condition (φ =180°). Temporally, the acoustic waves reveal a symmetric waveform lacking the abnormalities present when waves of unequal amplitude or phase interact and maintain a traveling wave component.

Second, the resonant frequencies of the sirens must be determined experimentally, as each unique siren will have its own characteristic peak amplitudes. This is best investigated using a frequency sweep method with each siren removed from the chamber. In this way, acoustic pressure is measured without regard to chamber resonance. An experimental frequency sweep was performed for 0 to 6 kHz and two peaks are observed at 3076 Hz and 5200 Hz for the left siren and 3084 Hz and 5101 Hz for the right siren. Wider bands of high sound production also exist at 1638-1915 Hz for the left siren and 1620-1860 for the right siren. These isolated frequencies offer three separate narrow bands of high amplitude acoustic excitation for each siren, while operating outside these bands results in much lower amplitudes.

Finally, a combined acoustic characterization of both sirens mounted inside the chamber must be completed to understand the system's performance. A frequency sweep from 0 to 6 kHz was employed with operation of sirens in-phase. To measure the frequency response of pressure oscillations within the chamber, a dynamic pressure transducer (Kulite model XCE-093-50D) was placed at the center of the chamber. When operating acoustic sources in-phase the chamber's center location represents a PAN, and is an excellent measure of the maximum pressure amplitude for a given frequency. The results of these measurements are shown in Fig. 11 for a chamber pressure of 400 psia (=2.76 MPa). Not all ten transverse chamber modes are identified in Fig. 12, with transverse resonance peaks only located near the sirens' optimum frequency bands. Although 1T and 2T modes exist for the chamber, for example, 1T and 2T modes do not appear in the comprehensive frequency sweep in Fig. 12 due to siren limitations, demonstrating the combined result of chamber and siren resonance.

In conclusion, the acoustic system demonstrates advantages over other techniques, but also has limitations. The piezoelectric sirens are useful only for select frequency bands. The pressure amplitudes achievable within these frequency bands are approximately equal to 1% of the mean chamber pressure. Although the pressure oscillations of LRE combustion instabilities can reach amplitudes far greater than 1% of the mean chamber pressure, the amplitudes obtained by this acoustic system are sufficient for inducing a significant response in the coaxial jet, as will be shown in the results and as shown in previous nonreacting experiments[16,17]. Further, by decoupling the source of chamber pressurization from propellant flow rates, it becomes advantageous to scale p' with a the coaxial jet dynamics rather than the mean chamber pressure. For example, p' may be scaled by the jet dynamic pressure. At any rate, the acoustic system provides three key advantages over other techniques. First, by spacing the sirens very far apart (0.82 m), several different T modes can be achieved below 6 kHz. For example, Fig. 12 shows that a mean chamber pressure of 400 psia allows one to produce a resonant mode at 1543 Hz (3T) and also at 3169 Hz (6T). Second, the pressure amplitude is directly controlled by altering the voltage input to the sirens, similar to a traditional loudspeaker. Last, both a PN and a PAN can be located at the jet by operating the sirens out-of-phase and in-phase, respectively.

D. High-Speed Imaging

Jet flow visualization is the primary diagnostic tool for studying nonreactive flow dynamics, provided by back-lit high-speed images. A variable power Newport model 66986 power supply controls a 300 W Xe lamp, which emits light in the near ultraviolet spectrum. This beam is projected through the rear window as a back-light source. Although the beam is not collimated, this back-lighting technique produces sufficient contrast at fluid interfaces. Differences in the refractive index of the jets and the surrounding medium provide the necessary distinction between the fluids of interest. The low temperature, liquid nitrogen inner jet appears as a dark column of fluid as viewed by the high-speed camera placed on the opposite side of the light source.

A Phantom v7.10 high-speed camera is used to visualize the fast dynamical processes inherent to an unforced coaxial jet flow as well as those present during high-frequency acoustic forcing. A 200 mm Nikon MicroNikkor lens is used with a no. 1 close-up lens attachment, giving a spatial resolution of 30 μm per pixel. Image framing rates of 10 kHz or greater are used in order to avoid aliasing up to 5 kHz, which is much greater than the highest forcing frequency used in this study, 2600 Hz. An external trigger from the facility control system is used to start recording the image frames, which are synchronized with all other data using the coordinated universal time (UTC) stamp from an IRIG-B timecode generator.

The reactive imaging set up is designed to capture ultraviolet bands of flame radiation in order to isolate chemiluminescence of excited hydroxyl radicals near a wavelength of 308 nm. An oxygen-hydrogen flame also emits light in the visible spectrum due to photon emission from H_2O radicals, which is blocked using a UV bandpass filter with a center wavelength of 307.2 nm with a FWHM of 11.7 nm and peak transmission of 16.0%. The filter is mounted to a 105 mm Nikon UV-Nikkor lens. After passing through the filter and lens, light is captured using a Lambert Instruments HiCATT image intensifier, and the photocathode of the image intensifier was chosen to have a high quantum efficiency in the UV range. In order to project the intensified light onto the Phantom v7.10 high-speed camera, a relay lens is mounted in between the image intensifier and the camera.

III. Results

Results will be shown that demonstrate the facility capability for both nonreactive and reactive tests at a mean chamber pressure of 400 psia. First, nonreactive tests are performed using liquid nitrogen (LN_2) as the inner jet and gaseous helium (GHe) as the outer jet, which creates a outer-to-inner jet density ratio S similar to an oxygen-hydrogen LRE. The inner and outer jet temperatures are set to be approximately 120 K and 275 K, respectively, which gives $S = 0.009$. Sample images are shown in Fig. 13 for an unforced jet with an outer-to-inner momentum flux ratio J of 2. Fig. 13 demonstrates many shear-coaxial jet features using a series of snapshots which were acquired at a frame rate of 10 kHz, and a small field of view is added to increase the clarity of structures near the injector exit.

At the exit of the injector, a recirculation zone is easily distinguishable. Moving in the radial direction from the center of the jet, one first observes an interface between the liquid nitrogen inner jet and the recirculation zone formed between the inner and outer jets. This feature is labeled as (1) in Fig. 13. The width of the recirculation zone is equal to the inner post thickness t at the exit of the injector and converges to zero as the recirculation zone extends downstream. The recirculation zone results from a finite inner post thickness, separating near-field stability of this geometry from that of classical co-flowing streams (t=0) commonly used in linear stability theory[18,19].

Advancing farther in the radial direction, an outer shear layer is identified between the gaseous helium outer jet and the surrounding gaseous nitrogen. Although this interface is less distinguishable in analogous LN_2-GN_2 jet experiments[3,4], the LN_2-GHe jet shown in Fig. 13 reveals significant contrast between the light outer jet and the more dense ambient nitrogen ($\rho_c \approx 7\rho_{oj}$). At this interface, an outer shear layer instability is formed. Preliminary analysis of LN_2-GHe jets also indicates unique stability characteristics for the inner and outer shear layers, making this imaging technique particularly valuable when accompanied by image analysis techniques such as proper orthogonal decomposition[11,20] and dynamic mode decomposition[21,23].

Immediately downstream of the recirculation zone, a dynamic interface forms between the inner and outer jets. This interface, labeled as (4) in Fig. 13, is the most important feature of the jet for this particular set of experiments due to its importance in inner jet atomization and mixing. This region may be called the mixing layer or the inner shear layer, and the latter term is used here for continuity with other works. Additionally, the extreme contrast between the liquid inner jet with $\rho_{ij} \approx 500$ kg/m^3 and the light outer jet with $\rho_{oj} \approx 5$ kg/m^3 makes for straightforward image analysis because pixel intensity gradients are most steep at the inner shear layer. Near the recirculation zone, the inner shear layer appears as well-defined interfacial waves. Further downstream, the shear layer thickness increases and these waves develop into vortices.

Regarding coaxial jet behavior in acoustically forced conditions, Figs. 14 and 15 show several image samples for PN and PAN forcing, respectively. Comparing Fig. 14 and Fig. 15 reveals the qualitative differences between forcing a jet located at a PN and PAN, and the value of an experimental facility which can create each condition. A jet located at a PN, when responsive to acoustic forcing, is exposed to a periodic transverse velocity with an amplitude of u'. This caused the jet to take a sinusoidal shape[2,11]. The inner and outer jets are swept to the left during one-half of the acoustic period and then to the right during the remaining half of the acoustic period. A PAN, on the other hand, causes the jet to adopt an axisymmetric instability due to injector pulsation in the outer jet[3,17,23]. Preliminary results show that jets located at a PN are more susceptible to transverse acoustic forcing than jets located at a PAN.

The preliminary results shown in Figs. 13-15 are for $J = 2$, which is also used for preliminary reactive tests to offer a comparison. Reactive tests are performed using liquid oxygen (LO_x) as the inner jet and gaseous hydrogen (GH_2) as the outer jet, with an equivalence ratio φ of 1.36, which is equivalent to a mixture ratio MR of 5.9. As described earlier, a temperature conditioning process is required in order to reach stable, desired inner and outer jet temperatures. To begin a reactive test, this temperature conditioning process is performed using nitrogen as a surrogate in order to conserve propellant.

Fig. 16 shows a time-series plot of a LO_x-GH_2 test which begins after achieving stable temperatures in the inner and outer jet. Remote valves are used to switch from the nitrogen simulant supply to the propellant supply. Due to differences in viscosity, density, and heat conduction constants, alternating between nitrogen simulant flow and propellant flow causes small changes in mass flow rate and temperature. The difference between the process fluid temperature at the injector before and after the species transition was found to be highly dependent on both chamber pressure and mass flow rate. As can be seen by the propellant valve operations in Fig. 16, an oxygen "lead" technique is used at the beginning of the automated test sequence. More than 10 s after the oxygen supply valve is opened, the hydrogen supply valve is opened prior to triggering the ignitor. The time at which each propellant valve is opened is chosen such that each propellant reaches the injector, and thus replaces the nitrogen surrogate, at the desired point in time. Only milliseconds after hydrogen reaches the injector, a torch ignitor is triggered to ignite the propellant mixture. Note that since the chamber pressure is largely determined by a nitrogen chamber pressurization system, propellants are ignited after the chamber is pressurized. To ignite the propellant mixture at elevated pressures, a novel photoignition technique is used, and will be described in subsequent publications. After a burn duration of 6 s, the hydrogen valve is closed first, causing the flame to extinguish.

The test firing represented in Fig. 16 was captured with OH* chemiluminescence imaging, and Fig. 17 includes several image samples acquired near t =19.5 s. These images clearly resolve the evolution of burning structures as they convect downstream. The near-field region produces a non-premixed flame caused by the diffusion of hydrogen and oxygen at the inner shear layer. In the far downstream region, structures may break away from the main body of the flame, as shown in the fourth image of Fig. 17. Of utmost importance in combustion stability studies are the burning structures produced near the exit of the injector, which represent localized pockets of intense OH* chemiluminescence. Although OH* chemiluminsescence has been shown to be proportional to heat release[24], more recent studies highlight sources of inaccuracy when using OH* chemiluminescence to quantify heat release to turbulent flames[25]. Still, Fig. 17 allows one to conclude that unsteady heat release exists, and OH* chemiluminescence such as these may be used to make approximate conclusions regarding flame standoff distance and instability frequencies using image analysis algorithms, for example.

IV. Conclusion

A new facility has been constructed at the Air Force Research Lab at Edwards AFB, CA to experimentally investigate combustion stability for cryogenic propellants at high pressure. A widely variable test matrix may be achieved for nonreactive as well as reactive conditions by utilizing precise control of inner and outer jet temperatures and chamber pressure. Temperatures are controlled with an accuracy of ±1 K in a range spanning from 110 K to room temperature, while the mean chamber pressure is controlled using a secondary chamber pressurization flow which partially decouples chamber pressure from combustion. A pair of piezoelectric sirens is used to create acoustic pressure oscillations which simulate the pressure oscillations an LRE combustion instability. Proper control of the phase difference and frequency of the sirens allows one to produce transverse standing waves with a pressure node (PN) or pressure antinode (PAN) located at the coaxial jet. The response of a coaxial jet to this environment is studied using high-speed diagnostics in the form of dynamic pressure transducers, backlit imaging, and OH* chemiluminescence imaging. These experimental capabilities, as well as ongoing facility advancements, will allow researchers to fundamentally investigate combustion instabilities in a manner which is comparable to very few other facilities in existence today.

Acknowledgments

Support was provided by the Air Force Office of Scientific Research, project officer Mitat Birkan, and by AFRL Laboratory Revitalization Funds. Significant technical contributions to the design and construction of the facilty are gratefully acknowleged from Randy Harvey, Al Badakhshan, Foster Beasley, Claudia Heflin, John Hasier, Todd Newkirk, Jeff Muss, and Rory Davis. Advanced Mobile Propulsion Test (AMPT) LLC provided significant expertise in the design and implementation of the data acquisition and control system and Sierra Lobo, Inc on the design and construction of the oxygen heat exchanger.

References

[1]Schadow, K., and Gutmark, E., "Combustion instability related to vortex shedding in dump combustors and their passive control," *Progress in Energy and Combustion Science* Vol. 18, No. 2, 1992, pp. 117-132.

[2]Leyva, I.A., Chehroudi, B., and Talley, D., "Dark core analysis of coaxial injectors at sub-, near-, and supercritical pressures in a transverse acoustic field," *43rd AIAA/ASME/SAE/ASEE Joint Propulsion Conference and Exhibit*, Vol. 5, 275–282, 2007-5456.

[3]Leyva, I.A., Rodriguez, J.I., Davis, B.W., and Chehroudi, B., "Preliminary results on coaxial jet spread angles and the effects of variable phase transverse acoustic fields," *46nd AIAA Aerospace Sciences Meeting & Exhibit*, Reno, NV, 2008.

[4]Teshome, S., "Droplet Combustion and Non-Reactive Shear-Coaxial Jets with Transverse Acoustic Excitation," PhD thesis, University of California, Los Angeles, Department of Mechanical and Aerospace Engineering, March 2012.

[5]Hardi, J., "Experimental Investigation of High Frequency Combustion Instability in Cryogenic Oxygen-Hydrogen Rocket Engines," PhD thesis, The University of Adelaide, School of Mechanical Engineering, June 2012.

[6]Hardi, J., Oschwald, M., and Dally, B., "Acoustic characterisation of a rectangular rocket combustor with liquid oxygen and hydrogen propellants," *Proceedings of the Institution of Mechanical Engineers, Part G: Journal of Aerospace Engineering*, Vol. 227, No. 3, 2013, pp. 436–446.

[7]Richecoeur, F., "Experiments and numerical simulations of interactions between transverse acoustic modes and cryogenic flames," PhD thesis, Ecole Centrale Paris, November 2006.

[8]Richecoeur, F., Ducruix, S., Scouflaire, P., and Candel, S., "Effect of temperature fluctuations on high frequency acoustic coupling," *Proc. of the Combustion Institute*, Vol. 32, 2009, 1663–1670.

[9]Mery, Y., Hakim, L., Scouflaire, P., Vingart, L., Ducruix, S., and Candel, S., "Experimental investigation of cryogenic flame dynamics under transverse acoustic modulations," *Comptes Rendus Mecanique*, Vol. 341, 2013, 100–109.

[10]Yu, Y.C., Koeglmeier, S.M., Sisco, J.C., and Anderson, W.E., "Combustion instability of gaseous fuels in a continuously variable resonance chamber (CVRC)," 44th Joint Propulsion Conference and Exhibit, AIAA 2008-4657, 2008.

[11]Teshome, S., Leyva, I.A., and Talley, D.G., "Proper orthogonal decomposition analysis of shear-coaxial injector flows with and without transverse acoustic forcing," *JANNAF Joint Subcommittee Meeting*, Huntsville, AL, 2011.

[12]Hulka, J. and Hutt, J.J., Instability phenomena in liquid oxygen/hydrogen propellant rocket engines. V. Yang and W.E. Anderson, editors, *Progress in Astronautics and Aeronautics: Liquid Rocket Engine Combustion Instability*, pages 39–72. AIAA, 1995.

[13]Woodward, R.D., Pal, S., Farhangi, S., Jensen, G.E., and Santoro, R.J., "LOx/GH2 shear coaxial injector atomization studies: effect of recess and non-concentricity," *45th AIAA Aerospace Sciences Meeting and Exhibit*, pp. 1–22, 2007-571.

[14]Webster, A.G., "Acoustical impedence, and the theory of horns and of the phonograph," *Proceedings of the National Academy of Sciences*, Vol. 5, 1919, pp. 275–282.

[15]Pierce, A. D. *Acoustics: An Introduction to Its Physical Principles and Applications*. Acoustical Society of America, 1991.

[16]Graham, J., Leyva, I.A., Rodriguez, J.I., and Talley, D., "On the effect of a transverse acoustic field on a flush shear coaxial injector," AIAA 2009-5142.
[17]Rodriguez, J.I., Leyva, I.A., Graham, J., and Talley, D., "Mixing Enhancement of Liquid Rocket Engine Injector Flow," AIAA 2009-5143.
[18]Jendoubi, S. and Strykowski, P.J., "Absolute and convective instability of axisymmetric jets with external flow," *Physics of Fluids*, Vol. 6, 1994, 3000–3009.
[19]Yecko, P., Zaleski, S., and Fullana, J.-M., "Viscous modes in two-phase mixing layers," *Physics of Fluids*, Vol. 14, No. 12, 2002, 4115–4122.
[20]Arienti, M. and Soteriou, M.C., "Dynamics of free jets submitted to upstream acoustic modulations," *Physics of Fluids*, Vol. 21, No. 112104, 2009.
[21]Schmid, P.J., "Application of the dynamic mode decomposition to experimental data," *Experiments in Fluids*, Vol. 50, 2011, pp. 1123–1130.
[22]Jovanovic, M.R., Schmid, P.J., and Nichols, J.W., "Low-rank and sparse dynamic mode decomposition," *Center forTurbulence Research, Annual Research Briefs,* 2012, pp. 139–152.
[23]Baillot, F., Blaisot, J.-B., Boisdron, G., and Dumouchel, C., "Behaviour of an airassisted jet submitted to a transverse high-frequency acoustic field," *J. of Fluid Mechanics*, Vol. 640, 2009, pp. 305–342.
[24]Marchese, A.J., Dryer, F.L., Nayagam, V., and Colantino, R.O., "Hydroxyl radical chemiluminescence imaging and the structure of microgravity droplet flames," *Twenty-sixth Symposium (International) on Combustion*, 1996, pp. 1219–1226.
[25]Kojima, J., Ikeda, Y., and Nakajima, T., "Spatially resolved measurement of OH*, CH*, and C*2 chemiluminescence in the reactio zone of laminar methane/air premixed flames," *Proc. Comb. Inst.*, Vol. 28, 2000, pp. 1757–1764.

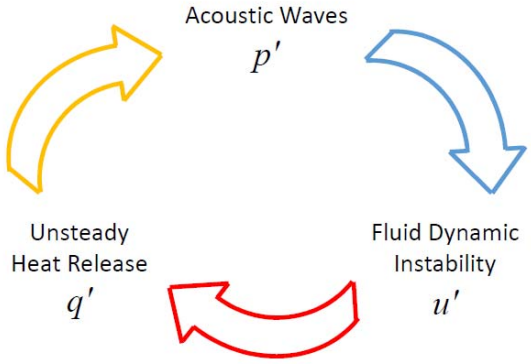

Figure 1. Three-part combustion instability feedback loop.

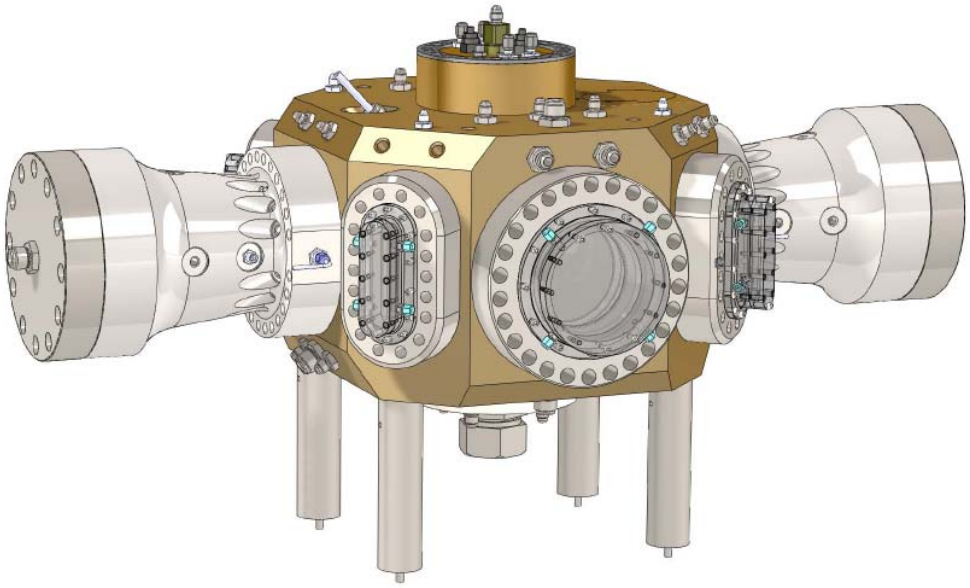

Figure 2. A three-dimensional CAD rendering of the high pressure combustion chamber at Air Force Research Laboratory at Edwards AFB, CA.

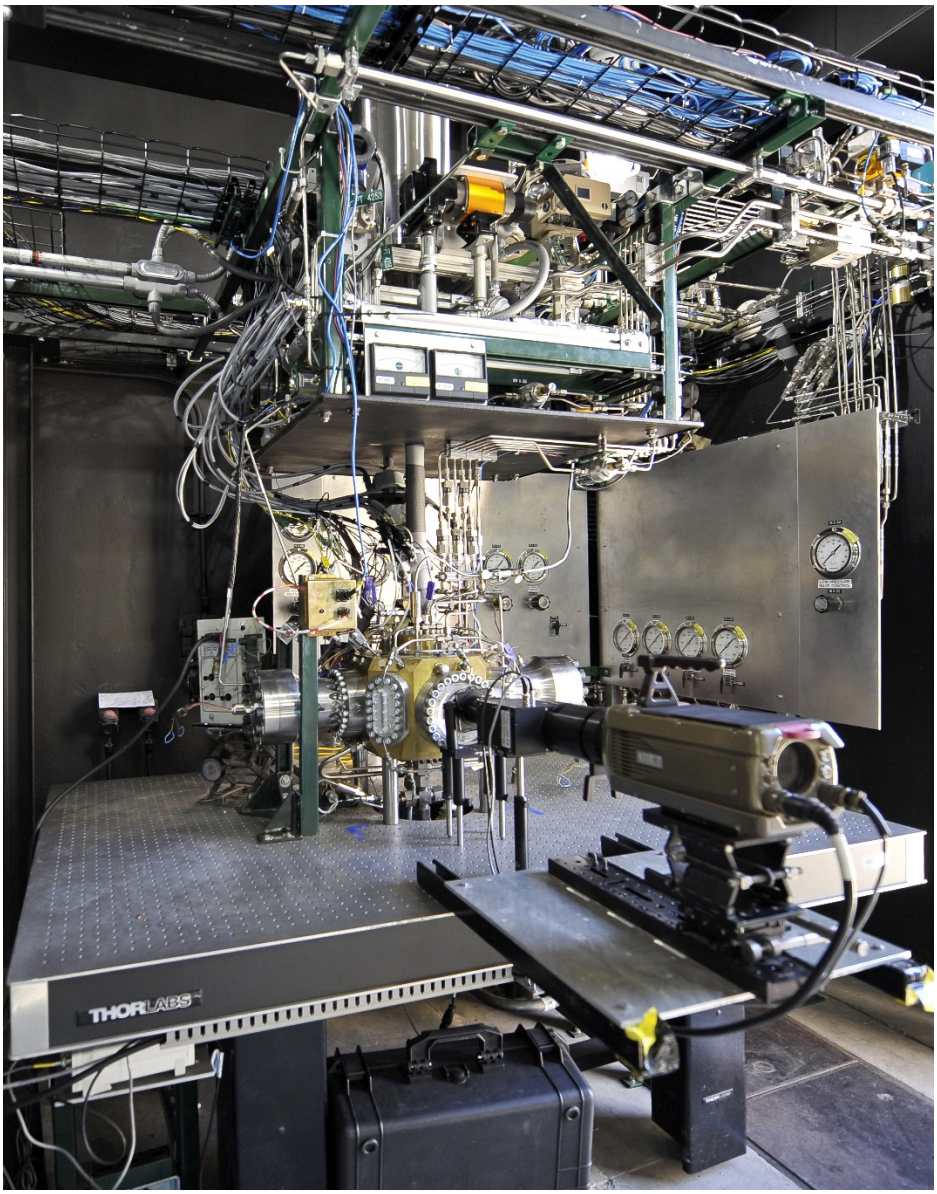

Figure 3. Photograph of the completed apparatus.

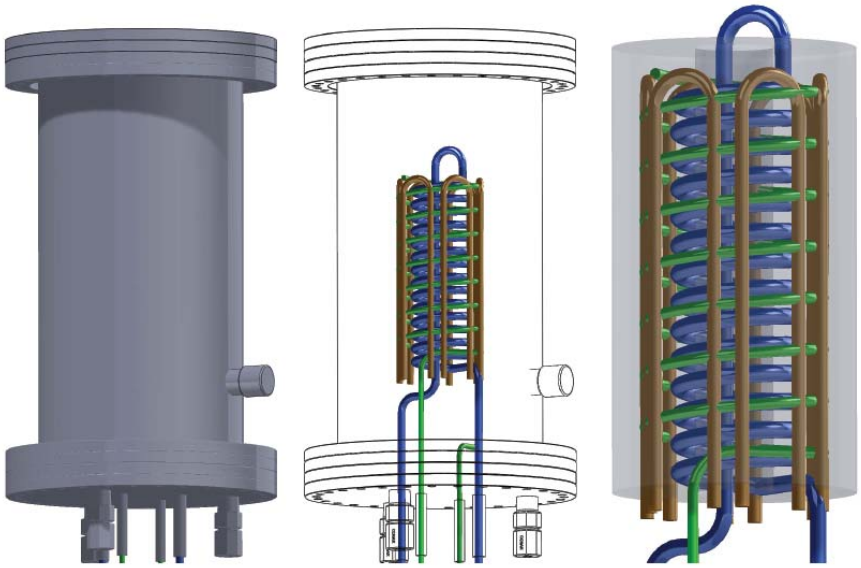

Figure 4. The oxygen heat exchanger cools oxygen gas (green) using liquid nitrogen (blue). Oxygen is cooled below the target temperature and electric heaters (brown) bring oxygen to the target temperature with a control resolution of ±1 K. Insulation is provided by a vacuum jacket (shown in left view, outlined in center view). An aluminum casting surrounds the plumbing assembly (shown in right view, gray).

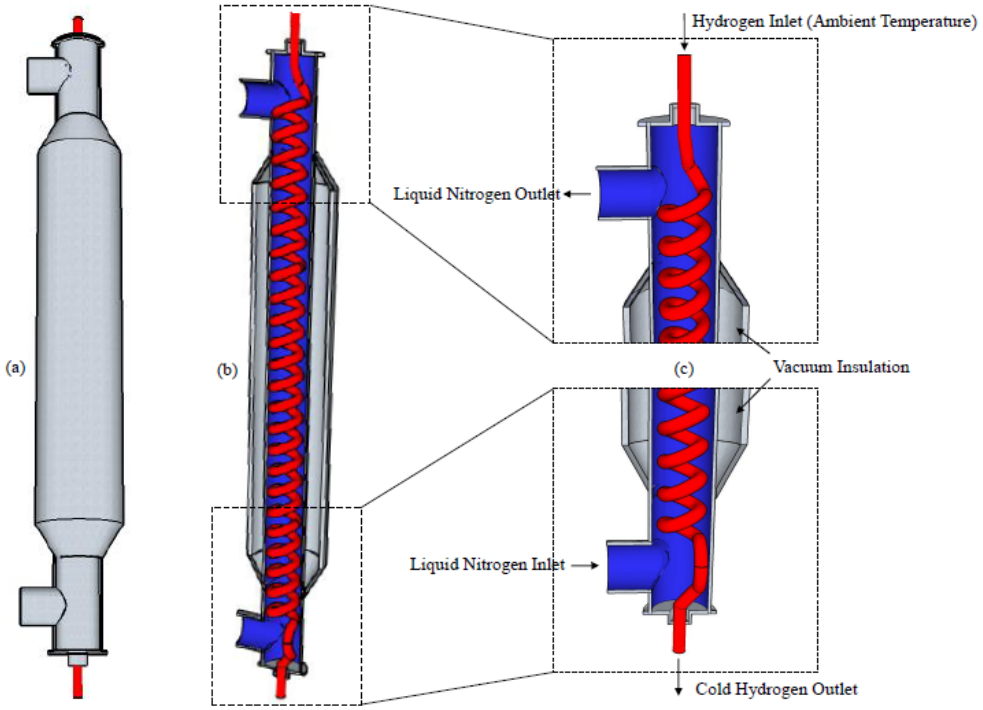

Figure 5. The hydrogen heat exchanger cools hydrogen gas (red) using liquid nitrogen (blue). Insulation is provided by a vacuum jacket.

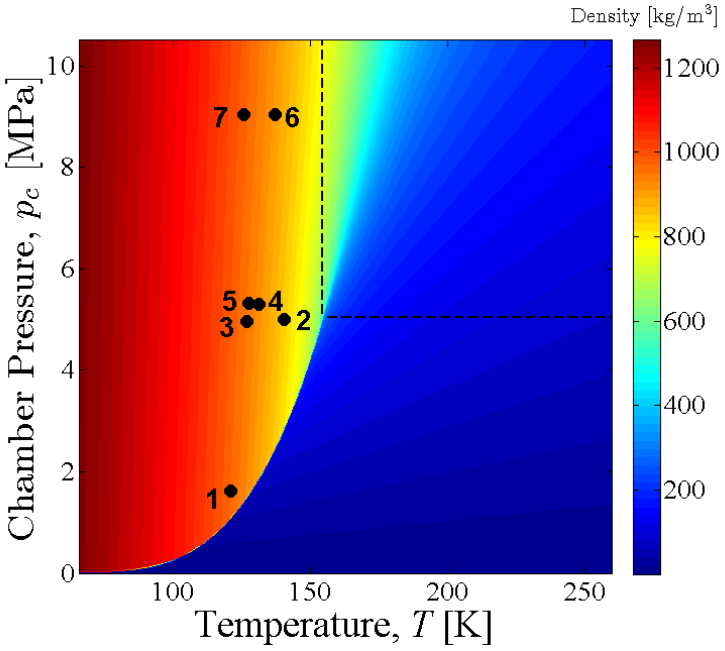

Figure 6. The facility's minimum achievable oxygen temperatures are plotted with an oxygen density contour overlay. Both chamber pressure and mass flow rate are controlled while temperature is measured. (1) 3.7 g/s (2) 2.6 g/s (3) 9.3 g/s (4) 3.0 g/s (5) 11.1 g/s (6) 2.7 g/s (7) 10.4 g/s

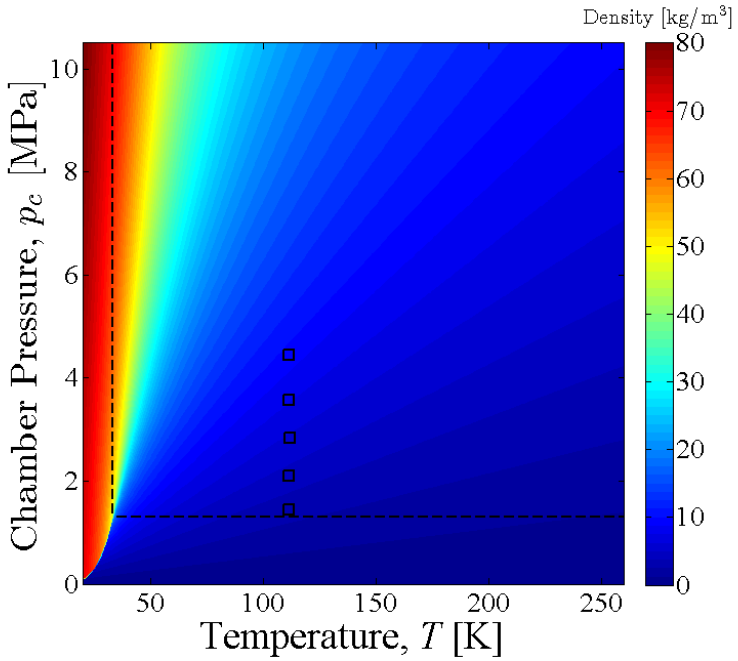

Figure 7. The facility's minimum achievable helium temperatures are plotted with a hydrogen density contour overlay. Helium is used as a surrogate gas, and is representative of minimum hydrogen achievable hydrogen temperatures in the outer jet. The nominal outer jet flow rate is approximately 1.3 g/s.

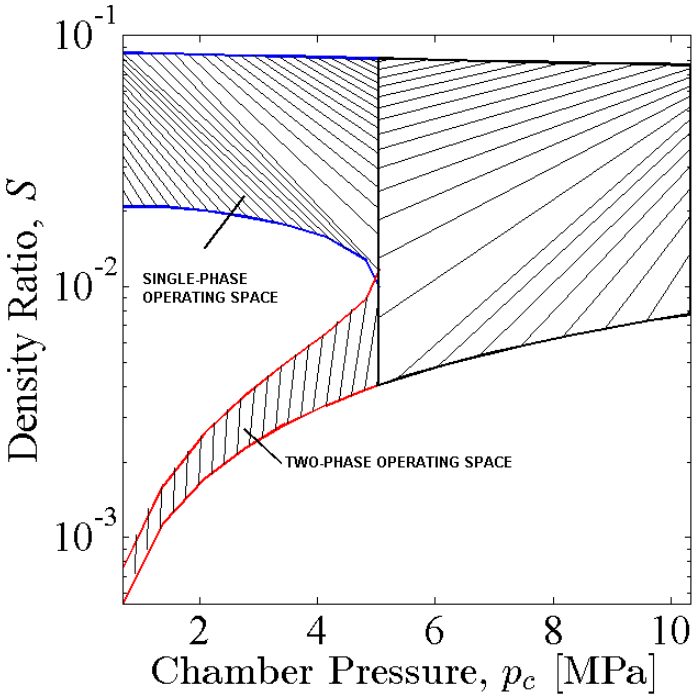

Figure 8. The facility's range of possible density ratios plotted versus chamber pressure.

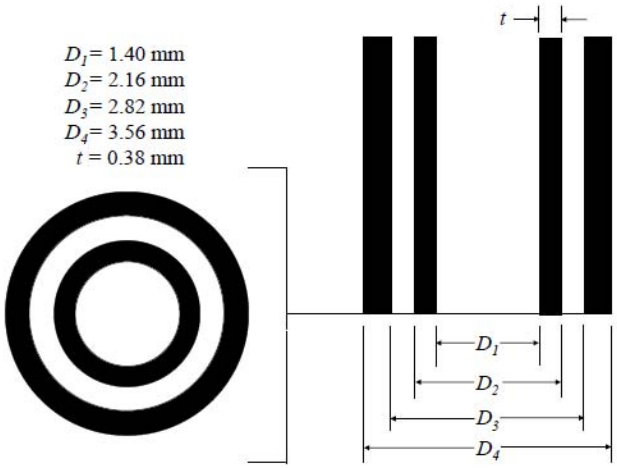

Figure 9. The dimensions of the coaxial injector used for new experiments in this study.

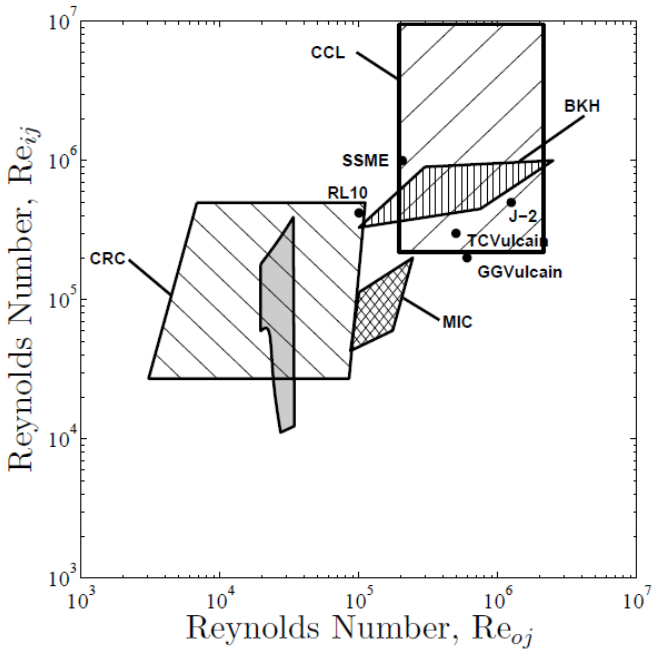

Figure 10. Shear-coaxial injector Reynolds numbers for the combustion stability facility (gray) with a comparison to other experimental facilities and liquid rocket engines with H2-O2 flows. Data is included for the Vulcain Gas Generator (GGVulcain), Vulcain Main Thrust Chamber (TCVulcain), RL10 engine, Space Shuttle Main Engine (SSME), J-2 engine, BKH combustor and Common Research Combustor (CRC) of DLR in Germany, Cryogenic Combustion Laboratory (CCL) of Pennsylvania State Univ., and the Mutli-Injector Combustor (MIC) of ONERA and CNRS in France.

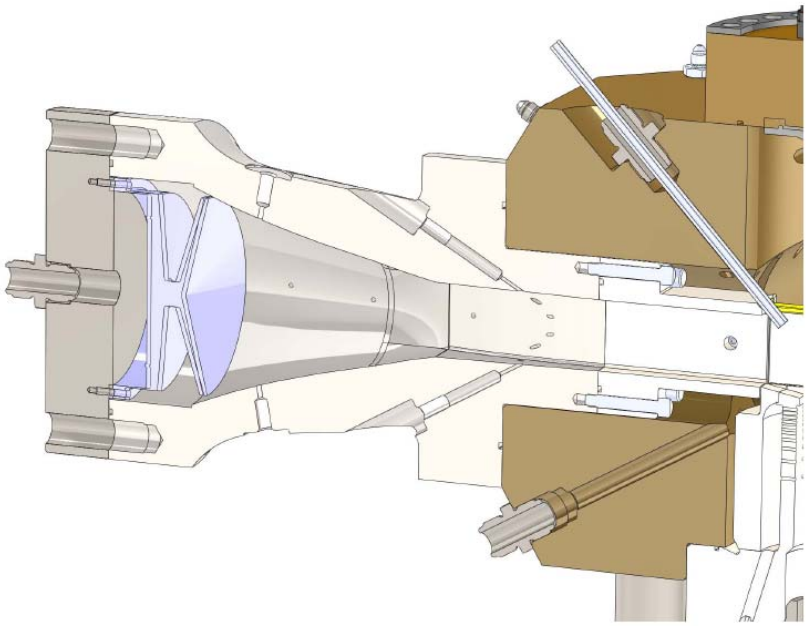

Figure 11. Cross sectional CAD rendering of the left waveguide. The end flange and piezoelectric siren are mounted on the left, and the waveguide assembly is mounted to the brass outer chamber on the right. The ignitor barrel enters through a diagonal port in the top left corner of the outer chamber wall.

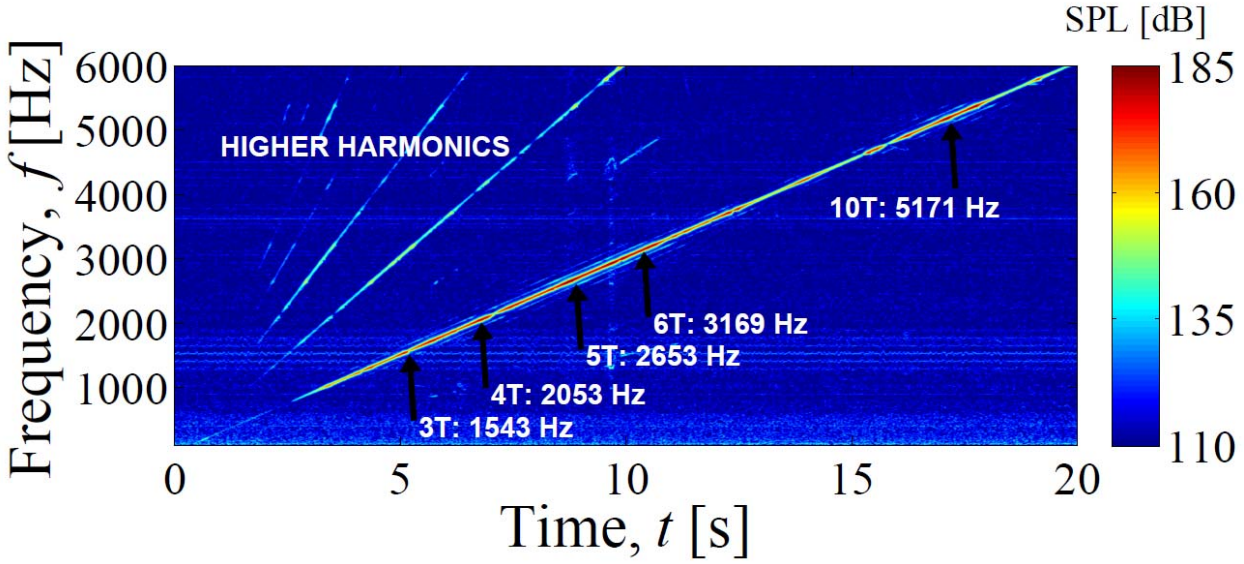

Figure 12. Acoustic pressure spectra results for a PAN condition measured using a pressure transducer in the center of the chamber. Magnitude is scaled with a sound pressure level (SPL) colormap, and key regions of transverse resonance are annotated. 1T, 2T, 7T, 8T, and 9T modes do not create appreciable pressure amplitudes, because these frequencies are outside of the useable frequency bands of the acoustic siresn. This study seeks to use one-dimensional, transverse waves only. Longitudinal modes and longitudinal-transverse mixed modes are ignored in this plot. p_c=400 psia = 2.76 MPa

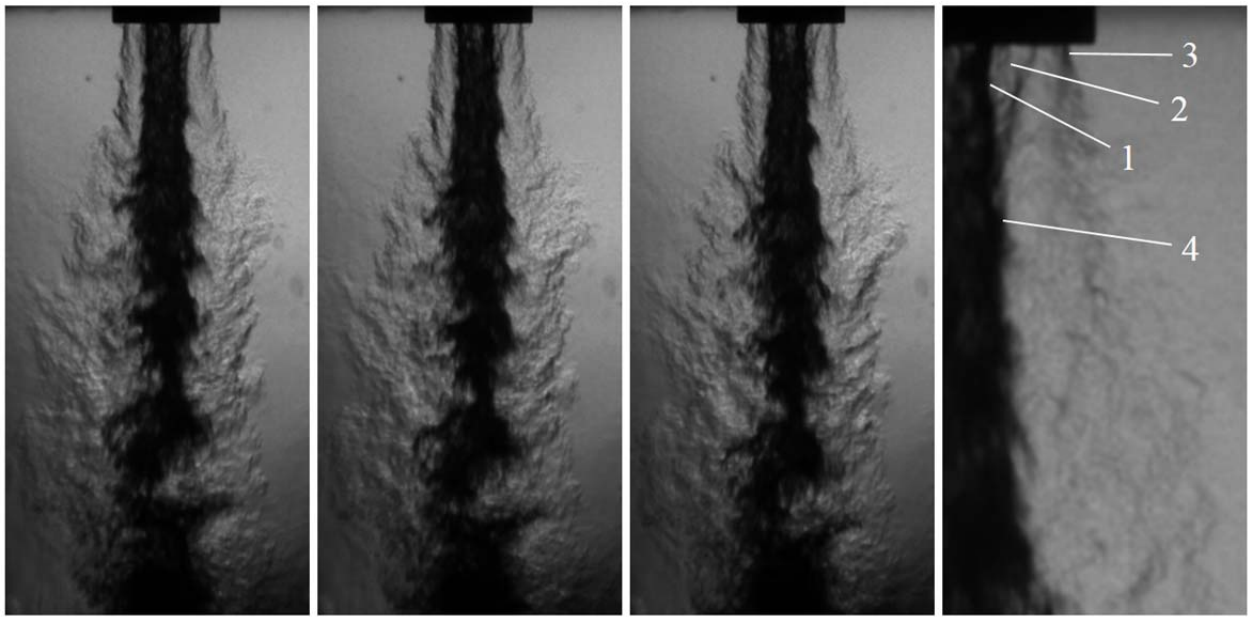

Figure 13. Liquid nitrogen-gaseous helium shear-coaxial jets without acoustic forcing. Three consecutive images are taken from a set of high speed images acquired at 10 kHz. A fourth image is shown with a reduced field of view to show the (1) interface between the inner jet and recirculation zone (2) recirculation zone (3) outer shear layer and (4) inner shear layer.
J = 2, p_c = 400 psia = 2.76 MPa

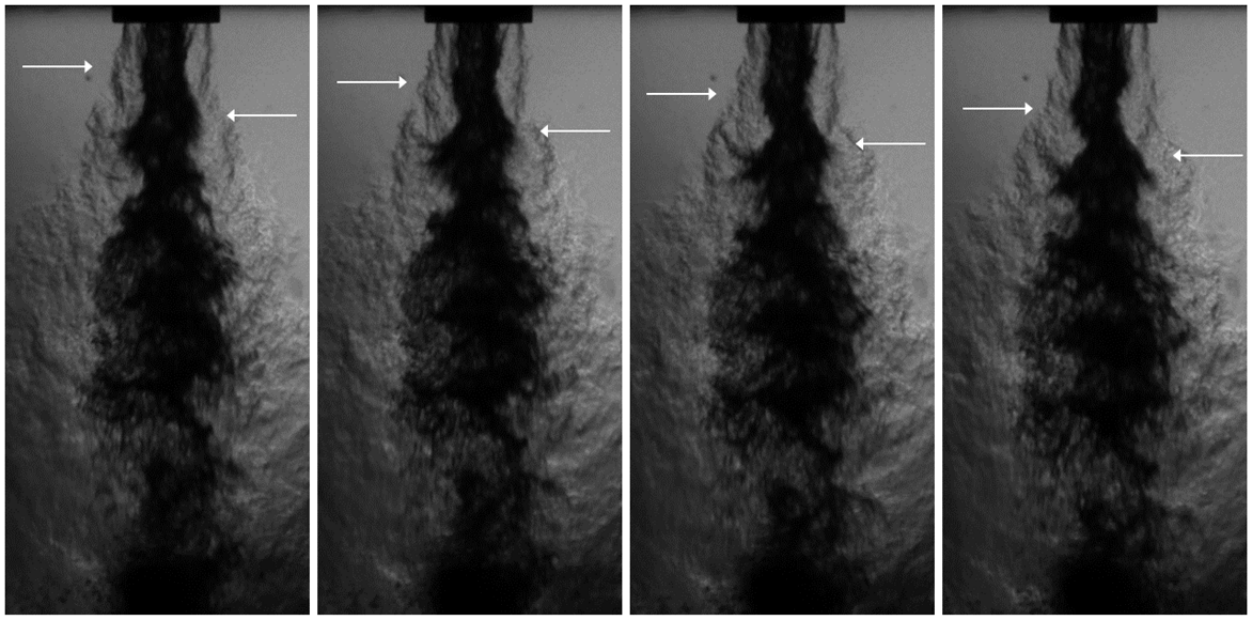

Figure 14. Liquid nitrogen-gaseous helium shear-coaxial jets exposed to external, transverse acoustic forcing at a pressure node. Four consecutive images are taken from a set of high speed images acquired at 10 kHz. An antisymmetric instability forms as periodic spanwise motions caused by the acoustic velocity perturbation u'. $J = 2$, $p_c = 400$ psia = 2.76 MPa, $f_F = 1700$ Hz, $u' = 0.43$ m/s

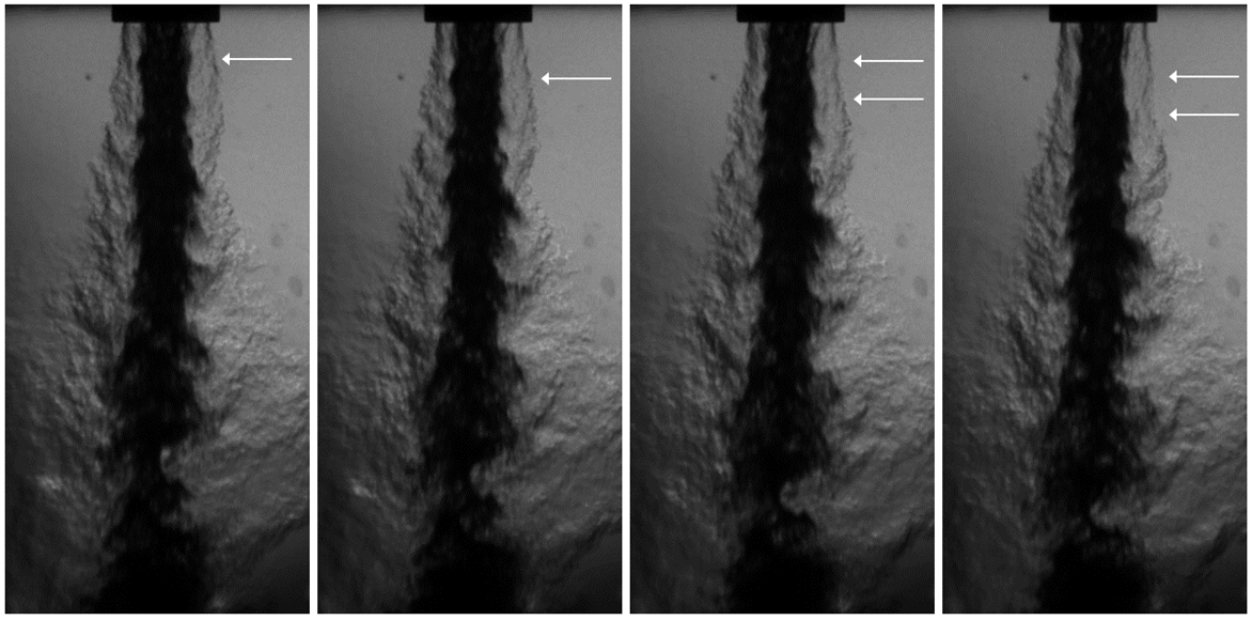

Figure 15. Liquid nitrogen-gaseous helium shear-coaxial jets exposed to external, transverse acoustic forcing at a pressure antinode. Four consecutive images are taken from a set of high speed images acquired at 10 kHz. An axisymmetric instability forms due to outer jet flow pulsations caused by the acoustic pressure perturbation p'. $J = 2$, $p_c = 400$ psia = 2.76 MPa, $f_F = 1700$ Hz, $p' = 1.53$ psi

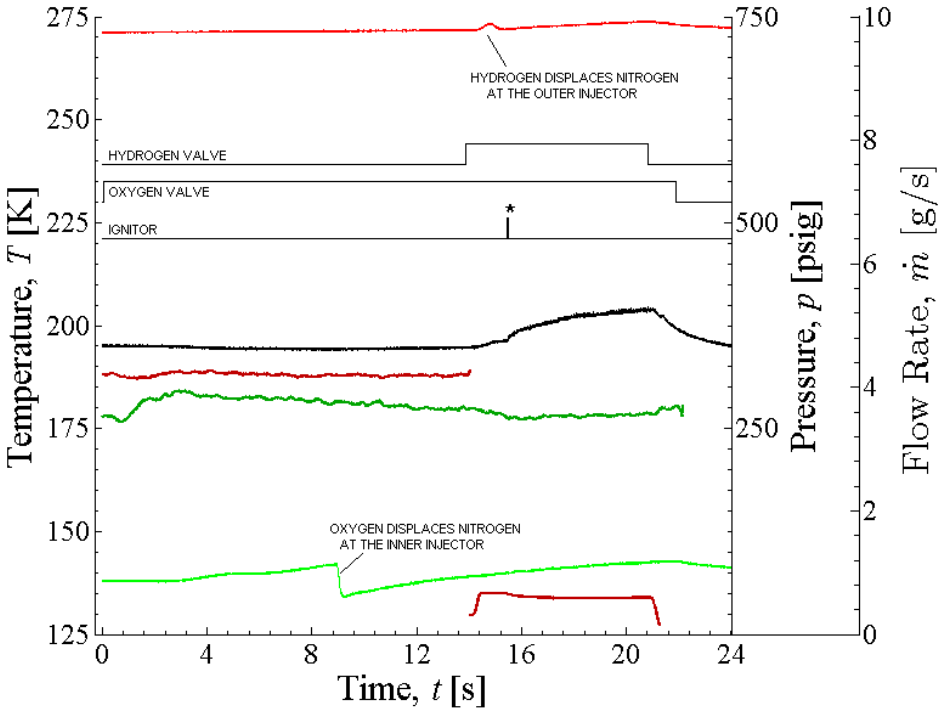

Figure 16. Time series plot of a typical reactive test using oxygen as the inner jet and hydrogen as the outer jet. The transition from a nitrogen simulant to the propellant occurs after the propellant valve is opened. A step change in outer jet mass flow rate occurs near $t = 14$ s, where nitrogen flow rate of approximately 4.2 g/s changes to a hydrogen mass flow rate of 0.65 g/s (dark red). The inner jet mass flow rate shows a species change near $t = 1$s, where a nitrogen flow rate of 3.6 g/s is overtaken by an oxygen mass flow rate of approximately 3.9 g/s. Inner jet temperature (light green), outer jet temperature (light red), and chamber pressure (black) are also shown. $MR = 5.9$ (φ=1.36), $J = 2$

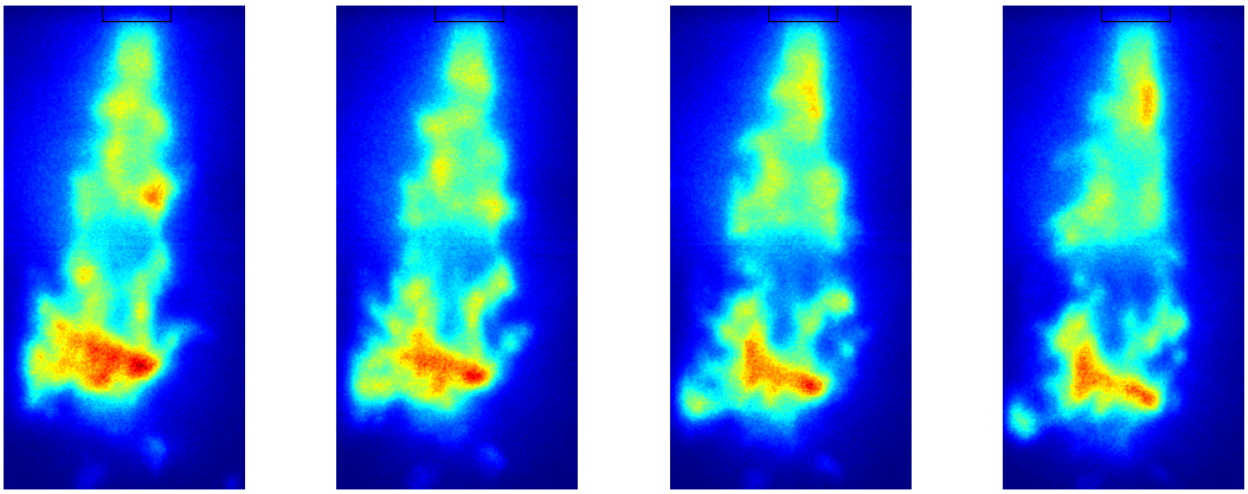

Figure 17. Liquid oxygen-gaseous hydrogen shear-coaxial jet flames without acoustic forcing. Four consecutive images are taken from a set of high speed images acquired at 16 kHz. The intensifier gate duration, which is essentially the camera exposure time, is set to 61 μs. Flame structures form near the injector exit and evolve as they travel downstream.
$MR = 5.9$, $J = 2$, $p_c \approx 400$ psia = 2.76 MPa